Three-dimensional scale-dependent Rayleigh-Taylor dynamics with variable acceleration in a finite-size domain: Part I. Solutions of bubbles in linear and nonlinear regimes

By H. Hwang AND S. I. Abarzhi†

1. Motivation and objectives

Rayleigh-Taylor instability (RTI) has been an active research area ever since Lord Rayleigh first questioned the instability of a simple system. This configuration is such that the plane-parallel layers of two fluids with unequal densities, where the heavier fluid is located above the lighter fluid, are under the constant gravity exerting downward (Rayleigh 1883). Moreover, Taylor considered not only a constant gravitational field but also the induced acceleration due to the pressure gradient (Taylor 1950). This insight led to the finding that the lighter fluid accelerating toward the heavier fluid has the equivalent effect of the previous case. As Mikaelian (2014) pointed out, Taylor's extension of the induced acceleration opened the new fields of RTI under time-varying acceleration, $g(t)$.

Rayleigh-Taylor (RT) flows with variable acceleration are prevalent among a broad spectrum of applications and natural phenomena (Abarzhi & Sreenivasan 2010; Abarzhi *et al.* 2013). Examples include atomization of a liquid jet in a crossflow (Rana & Herrmann 2011), blast-wave-driven RT mixing in core-collapse supernovae (Arnett 1996; Swisher *et al.* 2015), RT-unstable plasma irregularities in the Earth's ionosphere, and turbulent mixing and combustion (Peters 2000). However, information on RT dynamics under these conditions is limited. Swisher *et al.* (2015) conducted supernova experiments to see the interaction of the blast-wave-induced acceleration with the helium-hydrogen interface. Abarzhi *et al.* (2018) identified the properties of RT and Richtmyer-Meshkov (RM) dynamics with variable acceleration.

Prior theoretical studies often considered RTI in an infinitely extended domain in the direction of the acceleration. However, realistic applications have finite-size domains, and thus, the RT flow structures are bounded in space. Under the constant acceleration, Naveh *et al.* (2020) illustrate the effect of bounded space on the evolution of the 2D RTI. Also, Hwang & Abarzhi (2020) demonstrate the universal scaling for 2D RTI with time-varying acceleration to map solutions of the infinite domain to those of the finite domain.

Recently, remarkable success has been achieved in understanding the fundamentals of time-dependent RTI and RT mixing. Hill *et al.* (2019) discovered distinct subregimes of early-time dynamics depending on the time exponent of the acceleration. Moreover, Abarzhi & Williams (2020) identify in detail special solutions for bubbles and spikes in the nonlinear regime. Both works apply group theory to the hexagonal space group and the acceleration is assumed to be a power-law time-dependence in infinite domain.

† University of Western Australia, Australia.

As demonstrated by prior studies, the group theory works well in time-varying acceleration; it revealed the new mechanism for energy accumulation and transport at small scales (Swisher *et al.* 2015).

The present study aims to discover 3D RTI dynamics with time-varying acceleration in a finite-size domain. We apply the group theory to represent instabilities of the square pattern in 3D periodic flows. The dependence of RTI growth rate on the acceleration's parameters is identified in linear and nonlinear regimes. For the late-time nonlinear dynamics, we find a continuous family of asymptotic solutions, directly link the interface dynamics to the interface morphology and the interfacial shear, and derive the solutions for the regular bubbles. We also reveal the interfacial and multiscale character of the scale-dependent RT dynamics and analyze the mechanism of the transitions from the scale-dependent dynamics to the self-similar mixing for RT bubbles and for RT spikes.

2. Methodology

The group theory is applied to the subspace group p4mm for square 3D periodic RTI (Landau & Lifshitz 1987; Abarzhi 1996). Procedures to investigate the dynamics of p4mm follow those of pm11 2D RTI (Hwang & Abarzhi 2020). The governing equations are conservation laws of mass, momentum and energy. The acceleration follows a power-law in time $\mathbf{g}(t) = -Gt^a \hat{z}$. We solve the boundary value problem involving boundary conditions at the interface and at the outside boundaries of the finite-size domain. Readers are referred to Hwang & Abarzhi (2020) for a more detailed explanation of the methodology.

2.1. *Fluid potential*

For the space group p4mm, the fluid potentials are written as

$$\Phi_h(x,y,z,t) = \sum_{m,n=1}^{\infty} \Phi_{mn}(t) \left(z \sinh\left(m\alpha_{mn} L\right) + \frac{\cos\left(mkx\right)\cos\left(nky\right)}{m\alpha_{mn}} \cosh\left[m\alpha_{mn}(z-Z)\right] \right) + f_h(t) + c.c, \tag{2.1a}$$

$$\Phi_l(x,y,z,t) = \sum_{m,n=1}^{\infty} \widetilde{\Phi}_{mn}(t) \left(-z \sinh\left(m\alpha_{mn} Z\right) + \frac{\cos\left(mkx\right)\cos\left(nky\right)}{m\alpha_{mn}} \cosh\left[m\alpha_{mn}(z+Z)\right] \right) + f_l(t) + c.c, \tag{2.1b}$$

in a spatial coordinate system where $(x_1, x_2, x_3) = (x, y, z)$ such that x and y constitute the horizontal plane that is vertical to the acceleration and z represents vertical space. t denotes time. α_{mn} is defined as $\alpha_{mn}^2 = m^2 + n^2$ with integers $m, n = 1, 2, 3 \ldots$. Here, Φ_{mn} is the matrix of Fourier amplitudes with $\Phi_{mn} = \Phi_{nm}$ and $\Phi_{00} = 0$. $f_h(t)$ and $f_l(t)$ are time-dependent functions and $c.c$ are cross-terms. We note that the velocity $\mathbf{v}_{h,l}$ is related to the fluid potentials as $\mathbf{v}_{h,l} = \nabla\Phi_{h,l}$ and the continuity condition is automatically satisfied as $\Delta\Phi_{h,l} = 0$. Z is a size of the domain in the vertical direction.

2.2. *Interface symmetry*

Recall that the subspace group p4mm is applied to describe 3D periodicity of the flow. At the vicinity of the bubbles tip, the reflections in the x and y directions $x \to -x$

and $y \to -y$ as well as $(x, y) \to (-x, -y)$ are taken into account for p4mm. Moreover, not only the reflections but also the rotations on angles $\pm\pi/2$, $\pm\pi$ must be applied to Fourier series expansion. Therefore, the spatial expansions of interface $z^*(x, y, t)$ with the symmetry constraints only permit

$$z^*(x, y, t) = \sum_{i,j=0}^{\infty} \zeta_{i,j} x^{2i} y^{2j}. \tag{2.2}$$

2.3. *Dynamical system: 3D p4mm*

The moment expressions for M, Ns are introduced as

$$\{M, \widetilde{M}\}_{a,b,c} = \sum_{a,b,c=1}^{\infty} \{\Phi_{mn}(t), \widetilde{\Phi}_{mn}(t)\}(mk)^a (nk)^b (\alpha_{mn} k)^c \sinh(m\alpha_{mn} Z), \tag{2.3a}$$

$$\{N, \widetilde{N}\}_{a,b,c} = \sum_{a,b,c=1}^{\infty} \{\Phi_{mn}(t), \widetilde{\Phi}_{mn}(t)\}(mk)^a (nk)^b (\alpha_{mn} k)^c \cosh(m\alpha_{mn} Z). \tag{2.3b}$$

We note that additional weights appear for the Fourier matrix Φ_{mn} due to independent translational directions yet have the same magnitude of wavevectors $\mathbf{k}_1 = k$ and $\mathbf{k}_2 = k$.

Substitution of moment expressions in Eq. (2.3) and the interface expansion at the vicinity of the tips in Eq. (2.2) for the governing equation leads to the dynamical system equation for p4mm as

$$\dot{\zeta}_1 - (2N_{2,0,-1} + N_{0,0,1})\,\zeta_1 - \frac{M_{2,0,0}}{2} = 0, \quad \dot{\zeta}_1 - \left(2\widetilde{N}_{2,0,-1} + \widetilde{N}_{0,0,1}\right)\zeta_1 + \frac{\widetilde{M}_{2,0,0}}{2} = 0$$

$$(1+A)\left(\frac{\dot{N}_{2,0,0}}{2} + \zeta_1 \dot{M}_0 - \frac{N_{2,0,0}^2}{4} - g\zeta_1\right) = (1-A)\left(\frac{\dot{\widetilde{N}}_{2,0,0}}{2} - \zeta_1 \dot{\widetilde{M}}_0 - \frac{\widetilde{N}_{2,0,0}^2}{4} - g\zeta_1\right)$$

$$M_0 + \widetilde{M}_0 = 0. \tag{2.4}$$

Due to the additional weights, various choices of parameter sets a, b, c are possible for p4mm moments. For conciseness, we replace the moments in the dynamical system in Eq. (2.4) with independent moments. From the definition of the moment expression for p4mm in Eq. (2.3), we easily notice that for any kind of moments the following is satisfied.

$$M_{a,b,c} = M_{b,a,c}. \tag{2.5}$$

Also, we can verify (Abarzhi 1996),

$$M_{a+2,b,c-1} + M_{a,b+2,c-1} = M_{a,b,c+1}. \tag{2.6}$$

Note that $k_1 = k_2 = k_3$ is assumed for the wavelength. Applying Eq. (2.5)-(2.6) to the moments in Eq. (2.4) results in two independents moments, $M_{0,0,1}$ and $M_{0,0,2}$, where

$$M_{0,0,1} = 2M_{2,0,-1} = M_{2,0,-1} + M_{0,2,-1}, \tag{2.7}$$

$$M_{0,0,2} = 2M_{2,0,0} = M_{2,0,0} + M_{0,2,0}. \tag{2.8}$$

Exploiting the independent set of moments, the dynamical system of p4mm is written as

$$\dot{\zeta_1} - 2N_{0,0,1}\zeta_1 - \frac{M_{0,0,2}}{4} = 0, \quad \dot{\zeta_1} - 2\widetilde{N}_{0,0,1}\zeta_1 + \frac{\widetilde{M}_{0,0,2}}{4} = 0$$

$$(1+A)\left(\frac{\dot{N}_{0,0,1}}{4} + \zeta_1\dot{M}_0 - \frac{N_{0,0,1}^2}{8} - g\zeta_1\right) = (1-A)\left(\frac{\dot{\widetilde{N}}_{0,0,1}}{4} - \zeta_1\dot{\widetilde{M}}_0 - \frac{\widetilde{N}_{0,0,1}^2}{8} - g\zeta_1\right)$$

$$M_0 + \widetilde{M}_0 = 0. \tag{2.9}$$

2.4. *Truncation of Fourier amplitudes*

Analytical solutions describing 3D RT dynamics can be derived from the dynamics systems in Eq. (2.9) with proper truncation of Fourier amplitudes. We note that the approximation for the Fourier amplitudes is arbitrary. For example, retaining Fourier amplitudes to the second harmonic for pm11 leaves Φ_1, Φ_2 for heavier fluids and $\widetilde{\Phi}_1$, $\widetilde{\Phi}_2$ for lighter fluids (Hwang & Abarzhi 2020). Following the dimensional analysis on the solution, these Fourier amplitudes as a function of the curvature ζ_1 form a one-parameter family of solution. In addition, for p4mm, this choice of freedom allows not only the extent of the harmonic kept in the Fourier expansion but also the elements in the Fourier matrix of the same order.

More specifically, the Fourier matrix Φ_{mn} has two-dimensional elements depending on the row and column index m and n. As the matrix index increases, more unknowns in the dynamical system are introduced. In order to retain four unknowns, different sets of Fourier amplitudes can be considered, for instance, $(\Phi_{10}, \Phi_{20}, \widetilde{\Phi}_{10}, \widetilde{\Phi}_{20})$ and $(\Phi_{10}, \Phi_{11}, \widetilde{\Phi}_{10}, \widetilde{\Phi}_{11})$. Therefore, the choice of the elements in the Fourier matrix requires that all possible choices are compared and justified.

For this purpose, Abarzhi & Inogamov (1995) and Abarzhi (1996) address this justification for the ideal family of solutions for spatially periodic solutions of RTI. Let such a family of solutions exist and be unique; then there must exist a functional limit with respect to the free parameter (e.g., the curvature ζ_1) of the Fourier amplitudes Φ_{mn} as the order N of the approximation increases

$$\{\Phi(\zeta_1)\} = \lim_{N\to\infty}\{\Phi(\zeta_1)\}_N, \tag{2.10}$$

Also, the previous studies demonstrated the smoothness of the family solutions. This smoothness implies the convergence of the Fourier harmonics as the order increases $N \to \infty$ within the functional limits set by the free parameter,

$$|\Phi_{mn}|_{m+n=l+1} \ll |\Phi_{mn}|_{m+n=l}. \tag{2.11}$$

Thus, the absolute value of the amplitude Φ_{mn} decays exponentially as l increases. Moreover, since the choice of approximation order is arbitrary, the solutions corresponding to each approximation should be similar. In other words, no significant difference is observed between Φ_{11} and Φ_{20} (Abarzhi & Inogamov 1995). Therefore, we justify our choice of Fourier moments for p4mm as Φ_{10}, Φ_{20}, $\widetilde{\Phi}_{10}$ and $\widetilde{\Phi}_{20}$ in the present study.

3. Results

Our methodology arrives at the dynamical system in Eq. (2.4) which is consistently applied to both linear and nonlinear regimes for all Atwood numbers of the range,

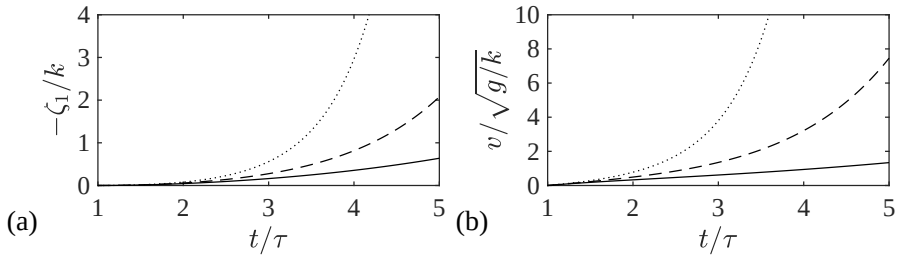

FIGURE 1. The linear regime solutions for the (a) curvature ζ_1 and (b) velocity v for bubbles for the subspace group p4mm. The curvature and the velocity are shown for the Atwood number $A = 0.7$ with two different finite-size domains, $kZ = 5$ (black lines) and $kZ = 0.5$ (gray lines). The acceleration exponents are $a = -1$ (solid lines), $a = 0$ (dashed line) and $a = 1$ (dotted line).

$0 < A \leq 1$. In this section, we identify the dependence of the RTI growth-rate on the acceleration's parameters. For the late-time nonlinear dynamics, we find a continuous family of asymptotic solutions and identify a special family of solutions for 3D RTI bubbles.

3.1. *Early-time dynamics*

Curvature ζ_1 and velocity v at the tip of RT bubbles with the acceleration exponent $a > -2$ are derived from the assumptions that $(t - t_0) \ll \tau$ with $t \gg \tau$ and $t \gg t_0$, where $\tau = \tau_G$ (e.g., see Hwang & Abarzhi 2020). The small initial amplitude and velocity assumptions lead to the solution in the linear regime as

$$\xi = C_1 \sqrt{\frac{t}{\tau}} I_{\frac{1}{2s}} \left(\sqrt{A \tanh{(kZ)}} \frac{(t/\tau)^s}{s} \right) + C_2 \sqrt{\frac{t}{\tau}} I_{-\frac{1}{2s}} \left(\sqrt{A \tanh{(kZ)}} \frac{(t/\tau)^s}{s} \right) \quad (3.1)$$

$$v = -\frac{4}{k} \frac{\mathrm{d}\xi}{\mathrm{d}t}. \quad (3.2)$$

The dimensionless curvature $\xi = -\zeta_1/k$ and the velocity $v/\sqrt{g/k}$ for bubbles with an Atwood number $A = 0.7$ are shown in Figure 1. As the acceleration exponent a increases from $a = -1$ to $a = 1$, bubbles and spikes are more curved and faster. The effect of finite-size domain kZ on v and ξ is illustrated by comparing the black lines $kZ = 5$ and gray lines $kZ = 0.5$. v and ξ increase at a slower rate for the finite-size domain with a small kZ than for the finite-size domain with a larger kZ.

3.2. *Late-time dynamics*

A one parameter family of asymptotic solutions in the form of a power-law function is sought for p4mm RTI ($a > -2$). In order to derive asymptotic solutions, we assume the same scalings in time for curvature, moments and velocity as in Hwang & Abarzhi (2020). Also, recall the universal scaling mapping of the solutions from the infinite-size domain to the finite-size domain. Then, the dynamical system in Eq. (2.4) yields the velocity v and the shear Γ as

$$v_\infty = \mu \frac{\sqrt{2}}{k\tau} \left(\frac{t}{\tau} \right)^{\frac{a}{2}} (A\xi)^{\frac{1}{2}} (3 - 8\xi)(3 + 8\xi)\mathcal{D}, \quad \Gamma_\infty = \mu \frac{12\sqrt{2}}{\tau} \left(\frac{t}{\tau} \right)^{\frac{a}{2}} (A\xi)^{\frac{1}{2}} \mathcal{D}, \quad (3.3)$$

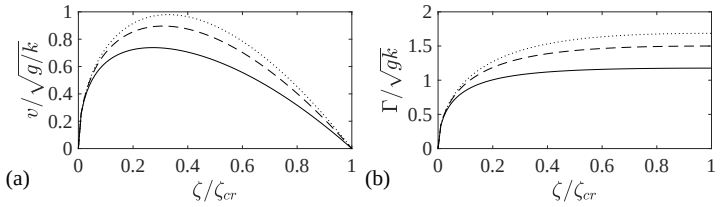

FIGURE 2. The nonlinear regime family of asymptotic solutions for the bubbles for p4mm subspace group. The velocity $v/\sqrt{g/k}$, the shear $\Gamma/\sqrt{gk}$ and the curvature ξ are shown with three different Atwood numbers, $A = 0.3$ (solid lines), $A = 0.6$ (dashed lines) and $A = 0.9$ (dotted lines).

where $\mathcal{D}$ is defined as $\mathcal{D} = \left\{48\xi - A(9 + 64\xi^2)\right\}^{-1/2}$. Also, the subscript ∞ denotes the solutions in the infinite-size domain. Moreover, the Fourier amplitudes are

$$\Phi_{1\infty} = \frac{-4\sqrt{2}}{k\tau}\left(\frac{t}{\tau}\right)^{\frac{a}{2}} (A\xi)^{\frac{1}{2}} (3 - 8\xi)(1 + 4\xi)\mathcal{D} \tag{3.4a}$$

$$\Phi_{2\infty} = \frac{\sqrt{2}}{k\tau}\left(\frac{t}{\tau}\right)^{\frac{a}{2}} (A\xi)^{\frac{1}{2}} (3 - 8\xi)(1 + 8\xi)\mathcal{D} \tag{3.4b}$$

$$\widetilde{\Phi}_{1\infty} = \frac{4\sqrt{2}}{k\tau}\left(\frac{t}{\tau}\right)^{\frac{a}{2}} (A\xi)^{\frac{1}{2}} (3 + 8\xi)(1 - 4\xi)\mathcal{D} \tag{3.4c}$$

$$\widetilde{\Phi}_{2\infty} = \frac{-\sqrt{2}}{k\tau}\left(\frac{t}{\tau}\right)^{\frac{a}{2}} (A\xi)^{\frac{1}{2}} (3 + 8\xi)(1 - 8\xi)\mathcal{D}. \tag{3.4d}$$

Similar to bubbles for pm11, bubbles move upward $v > 0$ and concave down $\zeta_1 < 0$. Thus, $\mu > 0$ for bubbles. This similarity is not surprising because by the virtue of convergence of the Fourier amplitude, the dynamical system of p4mm retains almost the same form compared to that of pm11, which differs only in constant coefficients. The family solutions for bubbles and spikes in the nonlinear regime are illustrated in Figure 2.

The effects of the finite-size domain kZ and Atwood number A on the family solutions are compared in Figure 2. The relatively larger domain $kZ = 5$ (black lines) has a larger velocity, a smaller shear and a small range of permissible curvature than the relatively smaller domain $kZ = 0.5$ (gray lines). As the Atwood number varies, fluids with a higher contrasting density ($A = 0.9$, solid line) show faster velocity and larger shear than fluids with a similar density ($A = 0.3$, dotted line).

The properties of bubbles are rescaled by their maximum values in Figure 3. For example, the velocity v is normalized by the Atwood velocity, which has the fastest solution, $v_A = v_{max}$. Similarly, the curvature ζ_1 and the shear Γ are normalized by the critical curvature $\zeta_{cr} = \zeta_{max}$ and criticial shear $\Gamma_{cr} = \Gamma_{max}$. The universality of the nonlinear solutions for bubbles is demonstrated with three different Atwood numbers, $A = 1.0, 0.5, 0.1$. The dependence between the the interface dynamics, morphology and shear is shown. Moreover, the convergence behavior of the Fourier amplitude are presented in Figure 3(d). Since the first harmonic is always large in magnitude compared to the second harmonic, the nonlinear solutions for bubbles are convergent for the entire range of Atwood numbers $0 < A \leq 1$. Also, no singularity is found in the solutions as

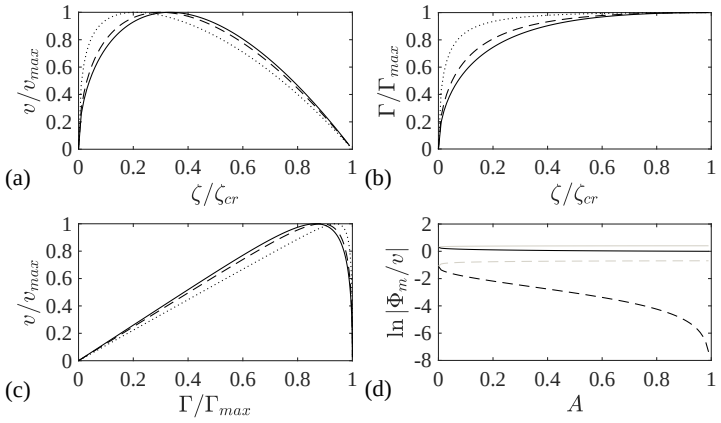

FIGURE 3. One-parameter family of asymptotic solutions for bubbles in the nonlinear regime for p4mm. The solutions are normalized by their maximum values. The velocity $|v/v_{max}|$ and the shear $|\Gamma/\Gamma_{max}|$ as a function of the curvature $|\zeta_1/\zeta_{cr}|$ are given in (a) and (b), respectively; (c) The 1-to-1 mapping of the rescaled velocity and shear. (d) The first two Fourier amplitudes are illustrated as a function of Atwood number A. The effect of the Atwood number $A = 1$ (solid line), $A = 0.5$ (dashed line) and $A = 0.1$ (dotted line) is shown. The Fourier amplitudes for heavy fluid (black lines) and light fluid (gray lines) are plotted for the first and second harmonics as a solid line and dashed line, respectively.

the bubble solutions are regular and stable. This regularity is in agreement with the experiment (Jacobs & Catton 1988).

3.3. *Special solutions*

The family solutions in the nonlinear regime in Eq. (3.3) describe all the possible velocity v and shear Γ at the tip of the bubble parameterized by curvature ξ. Thus, special solutions with specific properties for the diagnostic parameters can be identified from the general form. The specific properties include a particular value for the curvature or velocity. We note that the diagnostic parameters, velocity v, shear Γ and curvature ξ, are related to each other in the nonlinear regime (e.g., see Figure 3). Therefore, special solutions are characterized by one of the diagnostic parameters (e.g., ξ). These solutions found in the present work are the critical bubble, the convergence limit bubble, the Taylor bubble, the Layzer-drag bubble, the Atwood bubble and the flat bubble. From this point on, all the quantities presented herein are evaluated in the infinite domain.

3.3.1. *Critical bubble*

The critical bubble is defined as the bubbles with the maximum curvature ζ_{cr}. At $\zeta_1 = \zeta_{cr}$, the bubble velocity is zero $v_{cr} = 0$ and the shear Γ_{cr} achieves its maximum value Γ_{max}.

$$\zeta_{cr} = -\frac{3}{8}k, \quad v_{cr} = 0, \quad \Gamma_{cr} = \frac{1}{\tau}\left(\frac{t}{\tau}\right)^{\frac{a}{2}}\sqrt{\frac{6A}{1+A}}. \tag{3.5}$$

3.3.2. *Convergence limit bubble*

The convergence limit bubble is categorized as the bubbles whose curvature ζ_{cn} is at the limit of the convergence of the Fourier amplitudes. More specifically, the amplitudes in Eq. (3.4) satisfy $|\Phi_1| > |\Phi_2|$ at $\zeta_1 \in (\zeta_{cn}, 0)$ and $|\widetilde{\Phi}_1| > |\widetilde{\Phi}_2|$ at $\zeta_1 \in (\zeta_{cr}, 0)$, and

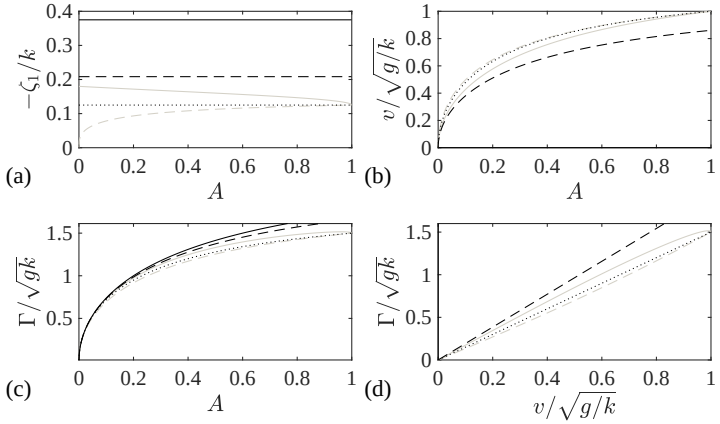

FIGURE 4. Special solutions for bubbles among the one-parameter family of asymptotic solutions with p4mm. (a) Curvature, (b) velocity and (c) shear are illustrated as a function of Atwood number A. A 1-to-1 relation between the shear and the velocity is presented in (d). Critical bubble (black solid), convergence limit bubble (black dashed), Taylor bubble (black dotted), Layzer-drag bubble (gray solid) and Atwood bubble (gray dashed).

also $|\Phi_1| = |\Phi_2|$ at $\zeta_1 = \zeta_{cn}$ for heavy fluid and $|\widetilde{\Phi}_1| = |\widetilde{\Phi}_2|$ at $\zeta_1 = \zeta_{cr}$ for light fluid. Therefore, the convergence limit bubble solution is expressed as

$$\zeta_{cn} = -\frac{5}{24}k, \quad v_{cn} = \frac{1}{k\tau}\left(\frac{t}{\tau}\right)^{\frac{a}{2}} \frac{14}{3}\sqrt{\frac{10A}{3(45+53A)}}, \quad \Gamma_{cn} = \frac{1}{\tau}\left(\frac{t}{\tau}\right)^{\frac{a}{2}} 9\sqrt{\frac{10A}{3(45+53A)}}. \tag{3.6}$$

To compare the convergence limit bubble to the critical bubble, the ratio of the curvatures is $\zeta_{cn}/\zeta_{cr} = 5/9$. For any Atwood number A, the convergence bubble is less curved than the critical bubble as its definition, thus implying the velocity is larger whereas the shear is smaller. The solutions for the velocity and curvature of the convergence limit bubble is illustrated in Figure 4.

3.3.3. *Taylor bubble*

The Taylor bubble has the curvature $\zeta_T = -1/8k$. The solution for the Taylor bubble was first derived in Davies & Taylor (1950) upon modifying the wavevector $k = 2\pi/\lambda$ to $k = 2\beta_1/\lambda$, where β_1 is the first zero of the Bessel function J_1. The Taylor bubble solutions are written as

$$\zeta_T = -\frac{1}{8}k, \quad v_T = \frac{1}{k\tau}\left(\frac{t}{\tau}\right)^{\frac{a}{2}} 2\sqrt{\frac{2A}{3+5A}}, \quad \Gamma_T = \frac{1}{\tau}\left(\frac{t}{\tau}\right)^{\frac{a}{2}} 3\sqrt{\frac{2A}{3+5A}}. \tag{3.7}$$

Only at $N = 1$ for the Taylor bubble is the second Fourier amplitude for heavy fluid zero $\Phi_2 = 0$. To compare the solutions to those for the convergence limit bubble, the curvature is less curved $\zeta_T/\zeta_{cn} = 3/5$, and thus, the Taylor bubble velocity is larger whereas the shear is smaller (e.g., see Figure 4).

3.3.4. *Layzer-drag bubble*

The Layzer-drag bubble is defined as the bubbles with velocity $v = (k\tau)^{-1}(t/\tau)^{a/2}$ $\sqrt{2A/(1+A)}$. These special solutions is called Layzer-drag bubble since the Layzer's first-order approximation for bubble velocity at $A = 1$ applies this velocity re-scaling (Layzer

1955). The experiments and the simulations are often compared to the Layzer-drag solutions. These special solutions are expressed as

$$\zeta_L = \zeta_L(k, A), \qquad v_L = \frac{1}{k\tau}\left(\frac{t}{\tau}\right)^{\frac{a}{2}}\sqrt{\frac{2A}{1+A}},$$
$$\Gamma_L = \frac{1}{\tau}\left(\frac{t}{\tau}\right)^{\frac{a}{2}} 12\left(9 - 64\left(\frac{\zeta_L}{k}\right)^2\right)^{-1}\sqrt{\frac{2A}{1+A}}. \tag{3.8}$$

The curvature of the Layzer-drag bubble is cumbersome and is given as $\zeta_L(k, A)$. The dimensionless curvature ζ_L/k is plotted as a function of A in Figure 4(a). However, simplified expression is only availabe at the end of the limits of the Atwood number A. At the limit of $A \to 1^-$, where the two fluids have highly contrasting densities, the solutions for the Layzer-drag bubble are

$$\zeta_L \approx -\frac{1}{8}k, \quad v_L \approx \frac{1}{k\tau}\left(\frac{t}{\tau}\right)^{\frac{a}{2}}, \quad \Gamma_L \approx \frac{1}{\tau}\left(\frac{t}{\tau}\right)^{\frac{a}{2}}\frac{3}{2}. \tag{3.9}$$

This results is the same solutions as for the Taylor bubble. At the limit of $A \to 0^+$, where the two fluids have very similar densities,

$$\zeta_L \approx -\frac{1}{8}k\sqrt{9-4\sqrt{3}}, \quad v_L \approx \frac{1}{k\tau}\left(\frac{t}{\tau}\right)^{\frac{a}{2}}\sqrt{2A}, \quad \Gamma_L \approx \frac{1}{\tau}\left(\frac{t}{\tau}\right)^{\frac{a}{2}}\sqrt{6A}. \tag{3.10}$$

The Layzer-drag bubble is less curved for the contrasting-density fluids $A \to 1^-$ than for the similar-density fluids $A \to 0^+$. For a finite density ratio $A \in (0, 1)$, the Layzer-drag bubble is related to the critical bubble and Taylor bubble as $\zeta_L/\zeta_{cr} \in (\sqrt{9-4\sqrt{3}}/3, 1/3)$ and $\zeta_L/\zeta_T \in (\sqrt{9-4\sqrt{3}}, 1)$, respectively. Similar to the previous analysis, the velocity for these special solutions is large whereas the shear is smaller than that for the Taylor bubble. The solution in Eq. (3.8) are presented in Figure 4.

3.3.5. *Atwood bubble*

As introduced earlier, the Atwood bubble is the bubble with the fastest velocity among the family of nonlinear solutions. In order to derive the curvature for Atwood bubble ζ_A, the characteristic equation for p4mm is sought as

$$4096A\xi_A^4 + 4096\xi_A^3 + 1152A\xi_A^2 - 27A = 0. \tag{3.11}$$

Recall that $\xi_A = -\zeta_A/k$ and $-\zeta_A < 0$ for the bubble. We find four roots by solving for Eq. (3.11), and only the roots that are positive in $A \in [0, 1]$ are chosen. Substitution of these roots for Eq. (3.3) leads to the velocity and shear expression for the Atwood number. However, they have a complex dependence on the Atwood number A; thus, they are illustrated in Figure 4) without the exact analytical expression.

Moreover, the invariant property of the Atwood bubble for p4mm is written using the fundamental scale (e.g., see Hwang & Abarzhi 2020),

$$\frac{1}{512}v_A^2(k\tau)^2\xi_A^{-3}\left(\frac{t}{\tau}\right)^{-a} = \left.\frac{\mathcal{S}_k^4}{\mathcal{S}_g}\right|_{Z\to\infty} = 1. \tag{3.12}$$

Similar to the solutions for the Layzer-drag bubble, solutions at the two end limits can be found in a rather simplified form. First, for fluids with highly contrasting densities

$A \to 1^-$, the solutions are

$$\zeta_A \approx -\frac{\{8-(1-A)\}}{64}k, \quad v_A \approx \frac{1}{k\tau}\left(\frac{t}{\tau}\right)^{\frac{a}{2}}\frac{\{16-3(1-A)\}}{16},$$

$$\Gamma_A \approx \frac{1}{\tau}\left(\frac{t}{\tau}\right)^{\frac{a}{2}}\frac{3\{32-7(1-A)\}}{64}. \tag{3.13}$$

These results are the same solutions as for the Taylor bubble and the Layzer-drag bubble at the same limit. This convergence of the three different solutions at $A = 1$ is shown in Figure 4. At the limit of $A \to 0^+$, where the two fluids have very similar densities,

$$\zeta_A \approx -\frac{3}{16}kA^{\frac{1}{3}}, \quad v_A \approx \frac{1}{k\tau}\left(\frac{t}{\tau}\right)^{\frac{a}{2}}\left(\frac{3}{2}\right)^{\frac{3}{2}}\sqrt{A}, \quad \Gamma_A \approx \frac{1}{\tau}\left(\frac{t}{\tau}\right)^{\frac{a}{2}}\sqrt{6A}. \tag{3.14}$$

For the finite fluid density ratio $A \in (0,1)$, the curvatures of the Atwood bubble are related to previous solutions as $\zeta_A/\zeta_{cr} \in (0,1/3)$, $\zeta_A, \zeta_L \in (0,1)$ and $\zeta_A/\zeta_T \in (0,1)$. The properties of the Atwood bubble properties are presented in Figure 4. As can be seen in the figure, the velocity is lareger and the shear is smaller for the Atwood bubble than for Layzer-drag and Taylor bubbles.

3.3.6. *Flat bubble*

The flat bubble is a stagnant bubble with zero curvature such that $v_f = 0$ and $\zeta_f = 0$. The flat bubble solution is expressed as

$$\zeta_f = 0,\ v_f = 0,\ \Gamma_f = 0. \tag{3.15}$$

We note that while the velocity is nonzero for both the critical bubble and the flat bubble, the curvature, and thus the shear, is zero only for the flat bubble.

3.4. *Transition to mixing*

Along the evolution of RTI, we demonstrated the properties of large coherent structures of RT bubbles characterized by the dominant scales. In the linear regime, the horizontal length scale, the wavelength k, serves as a single dominant length scale. In contrast, the two length scales, the amplitude ζ_1 and the wavelength k, become dominant length scales characterizing nonlinear regime solutions, thus manifesting multiscale behavior of RT in the late-time regime. After the linear and nonlinear regimes, which are scale-dependent regimes, it is known that RTI transits into a scale-invariant regime. In the scale-invariant regime, the vertical scale grows in a self-similar manner with time.

In a laboratory framework, the interface is described as $Y(\mathbf{r},t) = y_0(\mathbf{r},t)+y^*$, where y_0 is the location of the free surface and y^* is the interface distortion on the reference frame of the tip in Eq. (2.2). Then, the velocity is $v = \dot{z_0}$. The Atwood bubble solutions are the fastest solutions among the family of asymptotic solutions in the nonlinear regime. From Eq. (3.3), the velocity $v_a = v_{max}$ at the curvature $\zeta_1 = \zeta_A$ of the Atwood bubble satisfies

$$|\zeta_A| \sim k \sim \lambda^{-1}, \quad |v_A| \sim \frac{1}{k\tau}\left(\frac{t}{\tau}\right)^{\frac{a}{2}} = \left(\frac{g}{k}\right)^{\frac{1}{2}}. \tag{3.16}$$

Then,

$$|v| \sim \sqrt{G\lambda t^a} \qquad |y_0| \sim t\sqrt{G\lambda t^a}. \tag{3.17}$$

Following Eq. (3.12), the amplitude y_0 of the bubble grows as a vertical length scale

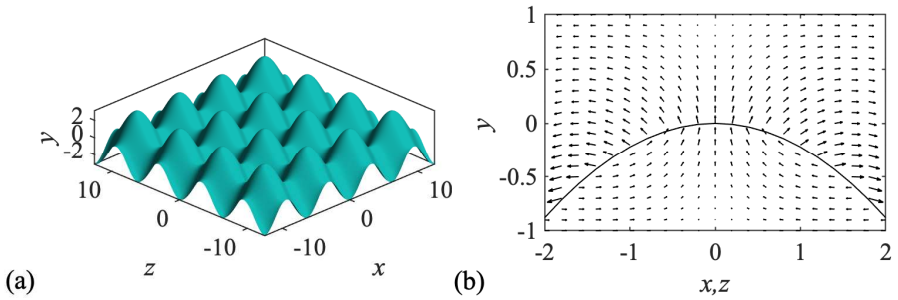

FIGURE 5. (a) Schematic view of the interface contour of 3D RTI for p4mm. (b) Qualitative velocity fields for planes at the tip of the bubble. The horizontal and vertical velocities are shown as a vector field and the interface is represented as a black solid line at $x = 0$, $y = 0$ planes.

comparable to the horizontal length scale λ. For $|y_0| > \lambda$, the vertical length scale becomes the dominant length scale characterizing the RTI. From the studies of the momentum model (Abarzhi 2010), the rate of loss of the specific momentum (i.e., the drage force per unit mass) scales as $\sim v^2/|y_0|$. Applying the transition of the dominant length scale from λ to $|y_0|$ shows the reduction of the drag force from $\sim v^2/\lambda$ to $\sim v^2/|y_0|$. This reduced drag force leads to the acceleration of the bubble and thus provokes the transition of RTI dynamics from scale-dependent to the self-similar mixing. By substituting λ in Eq. (3.17) for $|y_0|$, the scalings of the velocity $|v|$ and the amplitude $|y_0|$ imply

$$|v| \sim Gt^{a+1}, \qquad |y_0| \sim Gt^{a+2}. \tag{3.18}$$

3.5. *Flow fields*

The schematic view of the interface morphology is presented in Figure 5(a). We note that only the first Fourier harmonic is retained to provide the dominant mode shape. Similarly, the velocity field is inspected based on the fluid potential. The vectors and the solid line in Figure 5(b) show the velocity field and the interface with curvature $\zeta_1 = -0.22k$. The motion of the fluid is pronounced in the region near the interface. This observation suggests that the RTI is interfacial flow: intense motion of the fluid is observed in a vicinity of the interface, whereas the fluid motion is suppressed away from the interface.

Not only the interfacial property of the RTI but also the shear formed near the interface is well illustrated in Figure 5(b). Previous studies agree that the secondary instability is triggered due to the shear across the interface during RTI evolution. This secondary instability is in small-scale vortical structures and invokes shear-driven Kelvin-Helmholtz instability (KHI). The shear function Γ measures the intensity of the tangential velocity difference across the interface. Thus, Γ estimates the growth rate of KHI for bubbles and spikes as $\omega_{KHI} \sim \Gamma$ and $\widehat{\omega}_{KHI} \sim \widehat{\Gamma}$, respectively. Note that the nonlinear solutions for spikes are singular. This singularity $\Gamma \to -\infty$ as $\zeta_1 \to \zeta_A$ infers the possibility of the larger shear compared to the analytically predicted dynamics. On the other hand, nonlinear solutions for bubbles are regular. Since the growth rate of KHI is proportional to the shear $\omega_{KHI} \sim \Gamma$, the small-scale vortical structures are expected to be more pronounced for spikes than for bubbles.

4. Conclusions

The present work illustrates the scale-dependent dynamics of RTI under variable acceleration with a power-law time dependence. The group theory is applied to describe 3D spatially periodic RT flow in the plane normal to the acceleration. The square symmetry of the flow and the effect of the finite-size domain are considered for the first time. The irreducible representation of the flow potential is sought. Introducing moment expressions leads to the dynamical system for 3D RTI. Linear regime solutions follow the exponential form. Nonlinear regime solutions are derived as a continuous family of asymptotic solutions. Since the order approximation is an arbitrary choice, the choice of the Fourier amplitude is justified due to the demonstration of the amplitude convergence. The nonlinear regime solutions are directly related to the shear at the interface which triggers the small-scale vorticies. Also, the effect of the finite-size domain is presented with the fundamental scaling bridging the infinite solutions to the finite solutions. When fundamental scaling is applied, special solutions of RT bubbles are identified. From the Atwood bubble invariant, the multiscale character of 3D RTI is shown. Transition toward the mixing regime is addressed based on scaling analysis. The flow field predicted by the current approach demonstrates the interfacial characteristic of RTI, which is aligned with experiments.

REFERENCES

Abarzhi, S. I. & Inogamov, N. A. 1995 Stationary solutions in the Rayleigh-Taylor instability for spatially periodic flow. *J. Exp. Theor. Phys.* **80**, 132–143.

Abarzhi, S. I. 1996 Stationary solution of the Rayleigh-Taylor instability for spatially periodic flows: questions of uniqueness, dimensionality, and universality. *J. Exp. Theor. Phys.* **83**, 1012–1026.

Abarzhi, S. I. 2008 Review of nonlinear dynamics of the unstable fluid interface: conservation laws and group theory. *Phys. Scr.* **2008**, 014012.

Abarzhi, S. I. 2010 Review of theoretical modeling approaches of Rayleigh-Taylor instabilities and turbulent mixing. *Philos. Trans. R. Soc. A* **368**, 1809-1828.

Abarzhi, S. I. & Sreenivasan, K. R. 2010 Turbulent mixing and beyond. *Philos. Trans. R. Soc. A.* **368**, 1539–1546.

Abarzhi, S. I., Gauthier, S. & Sreenivasan, K. R. 2013 Turbulent mixing and beyond: non-equilibrium processes from atomistic to astrophysical scales. *Philos. Trans. R. Soc. A* **371**, 20120435

Abarzhia, S. I., Bhowmickb, A. K., Naveha, A., Pandianb, A., Swisherb, N. C., Stellingwerfc, R. F. & Arnettd, W. D. 2018 Supernova, nuclear synthesis, fluid instabilities, and interfacial mixing. *Proc. Camb. Philos Soc.* **51**, 162–178.

Abarzhi, S. I. & Williams, K. C. 2020 Scale-dependent Rayleigh–Taylor dynamics with variable acceleration by group theory approach. *Phys. Plasmas* **27**, 072107.

Arnett, D. 1996 *Supernovae and Nucleosynthesis*. Princeton University Press.

Davies, M. & Taylor, G. I. 1950 The mechanics of large bubbles rising through 1289 extended liquids and through liquids in tubes. *Proc. R. Soc. A* **200**, 375–390.

Dimonte, G. & Schneider, M. 1996 Turbulent Rayleigh-Taylor instability experiments with variable acceleration. *Phys. Rev. E* **54**, 3740.

Hwang, H. & Abarzhi, S. I. 2020 Two-dimensional scale-dependent Rayleigh-Taylor

dynamics with variable acceleration in a finite-size domain. *Annual Research Briefs*, Center for Turbulence Research, Stanford University, pp. 371–382.

Hill, D. L., Bhowmick, A. K., Ilyin, D. V. & Abarzhi, S. I. 2019 Group theory analysis of early-time dynamics of Rayleigh-Taylor instability with time varying acceleration. *Phys. Rev. Fluids* **4**, 063905.

Jacobs, J. W. & Catton, I. 1988 Three-dimensional Rayleigh-Taylor instability Part 2. Experiment. *J. Fluid Mech.* **187**, 353–371.

Landau, L. D. & Lifshitz, E. M. 1987 *Theory Course I-X*. Pergamon Press.

Layzer, D. 1955 On the instability of superposed fluids in a gravitational field. *Astrophys. J.* **122**, 1.

Meshkov, E. E. 2013 Some peculiar features of hydrodynamic instability development. *Philos. Trans. R. Soc. A* **371**, 20120288.

Mikaelian, K. O. 2014 Solution to Rayleigh-Taylor instabilities: bubbles, spikes, and their scalings. *Phys. Rev. E* **89**, 053009.

Naveh, A., Hill, D. L. & Abarzhi, S. I. 2020 Early- and late-time evolution of Rayleigh–Taylor instability in a finite-size domain by means of group theory analysis. *Fluid Dyn. Res.* **52**, 025504.

Olsona, D. H. & Jacobs, J. W. 2009 Experimental study of Rayleigh–Taylor instability with a complex initial perturbation. *Phys. Fluids* **21**, 034103.

Peters, N. 2000 *Turbulent Combustion*. Cambridge University Press.

Rana, S. & Herrmann, M. 2011 Primary atomization of a liquid jet in crossflow. *Phys. Fluids* **23**, 091109.

Rayleigh, L. 1883 Investigation of the character of the equilibrium of an incompressible heavy fluid of variable density. *Proc. R. Math. Soc.* **14**, 170–177.

Swisher, N. C., Kuranz, C., Arnettt, W. D., Hurricane, O., Robey, H., Remington, B. A. & Abarzhi, S. I. 2015 Rayleigh-Taylor mixing in supernova experiments. *Phys. Plasmas* **22**, 102707.

Taylor, G. I. 1950 The instability of liquid surfaces when accelerated in a direction perpendicular to their plane. *Proc. R. Soc. Lond. A* **201**, 192-196.